JOURNAL OF SPACECRAFT AND ROCKETS
Vol. 46, No. 1, January–February 2009

Visualization of a Capsule Entry Vehicle Reaction-Control System Thruster

P. M. Danehy,* J. A. Inman,† G. J. Brauckmann,‡ D. W. Alderfer,§ and S. B. Jones¶
NASA Langley Research Center, Hampton, Virginia 23681-2199
and
D. P. Patry**
Swales Aerospace, Hampton, Virginia 23681-2199

DOI: 10.2514/1.34846

Planar laser-induced fluorescence was used to visualize the reaction-control system jet flow emanating from the aft body of an Apollo-geometry capsule test article in NASA Langley Research Center's 31 in. Mach 10 Tunnel. The reaction-control system jet was oriented normal to the aft surface of the model and had a nominal Mach number of 2.94. The composition of the jet gas by mass was 95% nitrogen (N_2) and 5% nitric oxide (NO). The reaction-control system jet flow rate varied between 0 and 0.5 standard liters per minute, and the angle of attack and tunnel stagnation pressure were also varied. Planar laser-induced fluorescence was used to excite the NO molecules for flow visualization. These flow visualization images were processed to determine the trajectory and to quantify the flapping of the reaction-control system jet. The jet flapping, measured by the standard deviation of the jet centerline position, was as large as 0.9 mm, whereas the jet was 1.5–4 mm in diameter (full width at half-maximum). Schlieren flow visualization images were obtained for comparison with the planar laser-induced fluorescence. Surface pressures were also measured and presented. Virtual diagnostics interface technology, developed at NASA Langley Research Center, was used to superimpose and visualize the data sets. The measurements demonstrate some of the capabilities of the planar laser-induced fluorescence method and provide a test case for computational fluid dynamics validation.

Nomenclature

C_p = pressure coefficient
P_o = tunnel stagnation pressure
P_∞ = freestream static pressure
q_∞ = dynamic pressure

I. Introduction

A CAPSULE design following the heritage of Apollo was recently selected for NASA's Crew Exploration Vehicle (CEV) [1]. Capsules have some distinct advantages over lifting body shapes. They have a low structural weight (due to a low ratio of surface area to volume) and are less complex (typically no movable control surfaces). However, this reduced complexity comes at the expense of maneuverability [2]. Their smaller size allows them to be launched into space on the forwardmost point of a launch stack, a safer configuration compared with attaching the vehicle to the side of a rocket. Reaction-control system (RCS) jet thrusters offer the primary means for steering capsules both on-orbit and during planetary entry. RCS jets can be used to provide pitch, yaw, and roll control to change the direction of the capsule's lift vector during entry. This requirement is increasingly important for the CEV, as pinpoint ground (at Earth and, eventually, planetary) landings are planned for the CEV program. The accurate understanding and modeling of RCS jets, their trajectories, and their influence on the flowfield and therefore the moments acting on the vehicle are critical for designing and predicting the performance of new capsule-based space vehicles. In this paper, we use planar laser-induced fluorescence (PLIF) to qualitatively and quantitatively visualize an RCS jet for an Apollo-shaped capsule. The primary goal of this experiment was to demonstrate the capabilities of PLIF for visualizing RCS jets and for performing quantitative measurements. However, this data set may serve as a comparison case for computational fluid dynamics (CFD) simulations.

Although the CEV RCS strategy has not yet been clearly defined, it is useful to review the Apollo command module (CM) RCS to put the present work into context. The Apollo CM RCS was responsible for controlling the vehicle attitude from the point of separation from the service module until the parachutes were deployed before splashdown. The RCS was also designed to contribute to various crew abort scenarios. The Apollo RCS consisted of 12 maneuvering jets, four each for pitch, roll and yaw, all of which exhausted on the leeward side of the capsule [3]. The Apollo RCS jets were pressure fed and operated with hypergolic (self-igniting) propellants (N_2O_4 and monomethyl hydrazine), and the engines were designed to each produce 93 lb of thrust [3]. The converging/diverging jet nozzle had a 7:1 expansion ratio [3], resulting in a nominal Mach number of 3.5 (assuming $\gamma = 1.4$). The pressure in the combustion chamber was 150 psia [3]. The engines typically fired hundreds of times during a single mission, with burn times typically a fraction of a second but also lasting 1 min or longer [3]. The engine startup and shutdown times were on the order of 10 ms; thus, the startup and shutdown were short compared with typical firing durations [3].

One of the major goals of testing RCS jets in wind tunnels is to determine the interaction effects of the thruster plumes on the flowfield and vehicle surface pressures. To our knowledge, the Apollo program did not test for these interaction effects. Depending

Presented as Paper 1532 at the 44th AIAA Aerospace Sciences Meeting and Exhibit, Reno, Nevada, 9–12 January 2006; received 17 October 2007; revision received 1 March 2008; accepted for publication 14 March 2008.

*Research Scientist, Advanced Sensing and Optical Measurement Branch, MS 493. Associate Fellow AIAA.
†NASA Graduate Coop Student, Advanced Sensing and Optical Measurement Branch, MS 493; also Ph.D. Student, Department of Physics, College of William & Mary, Williamsburg, VA 23185. Student Member AIAA.
‡Test Engineer, Aerothermodynamics Branch, MS 408A. Member AIAA.
§Research Scientist, Advanced Sensing and Optical Measurement Branch, MS 493.
¶Optic and Electronic Technician, Advanced Sensing and Optical Measurement Branch, MS 493.
**Information Technology Specialist, MS 493.

on the jet characteristics and the local flowfield, the interaction effects can either augment or decrease thruster performance. These interaction effects can be obtained experimentally by testing a model in a wind tunnel with the thruster on (operational) and off, and subtracting the two results. The thruster is usually modeled using a simulant gas, matching the mass and jet-to-freestream momentum ratio and plume geometry. For simplicity, the RCS thruster can be simulated with cold N_2.

The NO PLIF method has been successfully applied in a variety of supersonic and hypersonic flow facilities [4–12]. Also, PLIF of I_2 has previously been performed in a hypersonic wind tunnel at NASA Langley Research Center [13] and elsewhere [14]. Previous studies of RCS jets in hypersonic flows, conducted using laser-induced fluorescence of iodine, are described in [15,16]. However, this paper reports the first application of NO PLIF in a hypersonic wind tunnel at NASA Langley Research Center. PLIF flow visualization was chosen for measuring the RCS jet flowfield for several reasons. First, alternate imaging techniques are either difficult to implement or are not likely to provide images of good contrast in this flow. For example, although the commonly used schlieren technique provides good visualizations of the forebody shock shape, it is not very sensitive in low-pressure wake regions such as that probed in this experiment, as will be demonstrated. Similarly, imaging the vehicle wake/jet region with Rayleigh scattering [17] would produce poor-quality images owing to the low density there. Particle-based velocimetry techniques such as particle image velocimetry [18] could be used, but the presence of particles could affect the flowfield or could clog the small RCS jet orifice. PLIF is ideally suited for visualizing RCS jets. Nitric oxide (NO) can be seeded directly into the N_2 jet gas simulant; because NO has nearly the same molecular weight as N_2, there is no question of particle or heavy molecule velocity slip or lag. However, NO is a toxic gas and must be appropriately handled. Though the quantities flowed in this experiment are relatively small, special safety precautions are taken when testing with NO. Unlike schlieren and Rayleigh scattering, whose sensitivity decreases with decreasing pressure, the NO PLIF signal intensity is approximately independent of pressure for a large range of low pressures. PLIF of the RCS jet yields strong signals with high contrast between the seeded jet fluid and the unseeded gas passing over the model. Another advantage of using PLIF for flow visualization is that it is relatively easy to perform velocimetry in hypersonic flows if a PLIF flow visualization is already being performed [19].

II. Experimental Description

The experiment was performed in the 31 in. Mach 10 Tunnel at NASA Langley Research Center. The test apparatus consisted of three main components detailed herein: the test model, the wind-tunnel facility, and the optical visualization systems.

A. Model Geometry

This model was designed and the experiment performed after U.S. President George W. Bush announced the Vision for Space Exploration in January 2004 but before the release of the CEV Exploration Systems Architecture Study (ESAS) in September 2005 [1]. During this time period, it was anticipated that the CEV would use a capsulelike entry vehicle, but the specific outer mold line contours were not known. Ultimately, the ESAS team chose an axisymmetric capsule closely resembling, but larger than, Apollo. This is the same generic shape used in the present experiment.

The model design was based on the Apollo geometry from various reports of that time. The heat shield radius is 1.2 times the diameter, the corner radius is 0.05 times the diameter, and the back-shell angle is 33 deg. The model is attached to a sting at a 28 deg angle, which was approximately the entry angle of attack of Apollo. Several pressure orifices (limited in number by the inside diameter of the sting) were placed on the model, as shown in Fig. 1, not only to measure model pressures but also to offer different seeding locations for the NO PLIF system. In addition to the standard surface orifices, an RCS plug and a porous plug were included. The RCS plug incorporated a conical nozzle with an expansion ratio that provided an exit Mach number of 2.94. The porous plug consisted of a sintered metal plug of 0.25 in. in diameter to diffuse the NO flow so as to not disturb the local flow. However, results obtained using this porous plug are not reported herein.

B. Planar Laser-Induced Fluorescence Imaging System

The PLIF system consists primarily of the laser system, beam forming optics, and the detection system. The laser system has three main components: a pump laser, a tunable pulsed dye laser, and a wavelength extender. An injection-seeded Nd:YAG laser (Spectra Physics Pro-230-10) operating at 10 Hz pumped the pulsed dye laser (Spectra Physics PDL-2), which contained a mixture of rhodamine 590 and 610 laser dyes in a methanol solvent. The output of the dye laser and the residual infrared from the Nd:YAG are combined in a wavelength extender (Spectra Physics WEX) containing both a doubling and a mixing crystal. These components are shown in Fig. 2: 1) Nd:YAG laser, 2) dye circulators, 3) wavelength controller for the 4) pulsed dye laser, 5) wavelength extender, and 6) low-pressure monitoring gas cell. The resulting output is tuned to a wavelength of 226.256 nm, chosen to excite the strongly fluorescing spectral lines of NO near the Q_1 branch head, where Q indicates that the change in the rotational quantum number is zero and the subscript 1 indicates both the upper and lower spin coupling.

A monitoring gas cell system is used to ensure that the laser is tuned to the correct spectral line of NO. The gas cell contains a low-pressure mixture of 5% NO in N_2. A quartz window serves as a beam splitter and sends a small portion of the laser energy through windows on either side of the gas cell. A photomultiplier tube monitors the fluorescence intensity through a third window at right angles to the path of the laser beam.

The components of this laser system are mounted within a two-level, enclosable, portable cart. A photograph of this portable PLIF system is shown in Fig. 2 with the panels removed to show the internal components. When all the panels are in place, a single monochromatic ultraviolet laser beam exits the cart, creating a relatively safe operating environment. Further details of the system can be found in [20].

For the experiments reported herein, this portable system was installed adjacent to NASA Langley Research Center's 31 in. Mach 10 Tunnel. A dedicated, adjustable scaffolding with attached mirrors and prisms directed the UV laser beam to the top of the wind-tunnel test section. Optics then formed the beam into a 100-mm-wide by ~1-mm-thick laser sheet, which was directed vertically

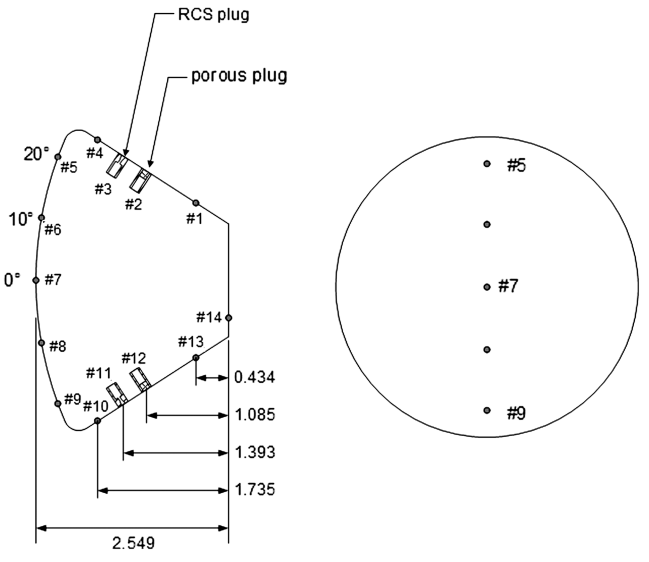

Fig. 1 Capsule design: a) side view, and b) front view. Measurement units are inches.

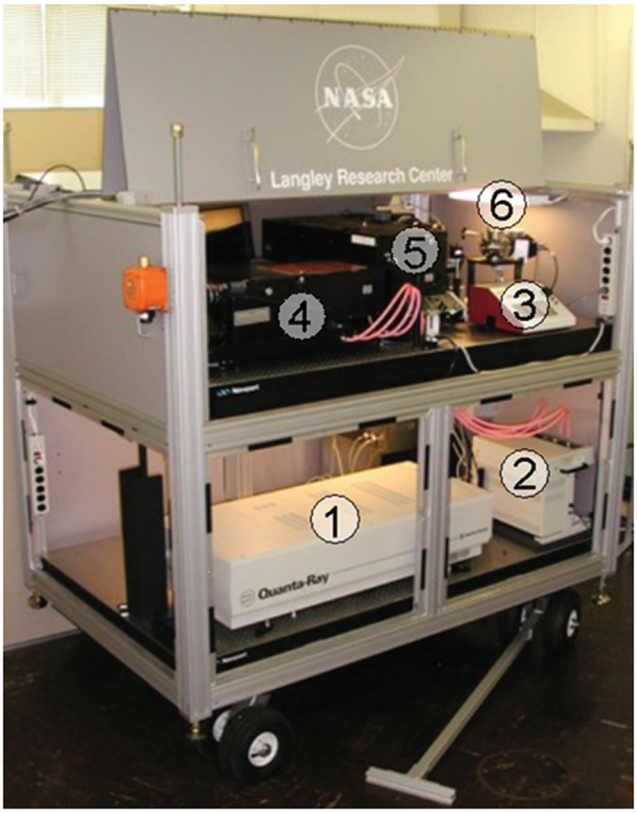

Fig. 2 The portable PLIF system, shown with panels removed.

downward through a window in the top of the test section. The section of scaffolding directly above the test section was mounted to a translation stage that could be remotely controlled so that the laser sheet could be swept spanwise through the flowfield during a tunnel run. This was used for the alignment of the laser sheet and also for scanning the image plane through the flowfield to visualize three-dimensional flow structures. The resulting fluorescence from NO molecules in the flow was imaged onto a gated, intensified charge-coupled device (CCD) camera at a viewing angle normal to the laser sheet. A 3-mm-thick Schott glass UG5 filter was placed in front of the camera lens to attenuate scattered light at the laser's frequency. This was particularly important when the laser sheet impinged on the surface of the model, potentially resulting in direct reflections toward the camera.

Flow visualization images were acquired at 10 Hz with a 1 μs camera gate and a spatial resolution of approximately 5–7 pixels/mm, varying from run to run as different camera views and laser sheet orientations were used. An image of a scale was obtained with the PLIF camera for the different camera placements so that the magnification could be determined in postprocessing. The temporal and spatial resolution was more than sufficient to resolve the flow structures of interest.

Sets of 100 single-shot images were acquired for most measurements. Background images were also acquired on each day of testing. During the acquisition of these background images, the laser was firing but no gas was flowing through the RCS jet. Any nonzero intensity in these background images is due to either camera dark current or laser scatter and room light not being blocked by the filter in front of the camera lens. Background images were created from the average of 100 single-shot images to smooth out random shot-to-shot variations in background intensity in postprocessing.

C. Schlieren

A vertically mounted lens schlieren system is used for flow visualization in the 31 in. Mach 10 Tunnel. The schlieren system consists of two 150-mm-diam, 1000 mm focal length achromatic lenses; a point light source; a knife edge; and a CCD video camera all mounted on an adjustable frame above and below the tunnel. High-quality polished windows above and below the test section of the tunnel provide optical access.

The light source used is an Oriel® 6427 Xenon Flashlamp with a 3 mm arc length. An Oriel® 68826 Flashlamp Power Supply is used to operate the flashlamp at 60 flashes per second with 800 mJ per flash. At these settings, the flash output has a duration of approximately 10 μs. The flashlamp is mounted in an Oriel® 60000 Series Q Housing that uses a condenser lens to image the light onto a 1-mm-diam pinhole. The flashlamp assembly is located 1 focal length away from the first 150-mm-diam lens to collimate the light through the tunnel. Below the tunnel, the second 150-mm-diam lens captures the entire collimated beam and focuses the light onto a knife edge mounted on a three-axis positioner. Just below the knife edge, a Hitachi KP-M1U monochrome CCD video camera is positioned to image the flow visualization during the test. Images are recorded on a PC with a frame grabber.

In the current configuration, the schlieren and PLIF systems cannot be used simultaneously. The schlieren was set up and used on repeated runs after the conclusion of the PLIF experiments. Because of the orientation of the schlieren system, the capsule model was rotated 90 deg about the sting axis to provide the schlieren images shown in this paper. All schlieren images were obtained with an angle of attack of the sting equal to 0 deg (model angle of attack of 28 deg).

D. Wind Tunnel, Operating Conditions, Mass Flow Control, and Data Acquisition Systems

The 31 in. Mach 10 Tunnel is an electrically heated blowdown facility located in Building 1251 at NASA Langley Research Center in Hampton, Virginia. A summary of the facility is provided here; for more details, see Micol [21]. As the name implies, the facility has a nominal Mach number of 10 and a 31 in. square test section. The tunnel uses heated, dried, and filtered air as the test gas. The air flows from the high-pressure heater, through the settling chamber, three-dimensional contoured nozzle, test section, second minimum, and aftercooler, and into vacuum spheres pumped by a steam ejector and conventional vacuum pumps. The test section is "closed," as opposed to an "open jet" test section. Large windows form three walls (including the top and bottom) of the test section, with the fourth wall formed by the model injection system. This window arrangement has advantages in the present experiment because the laser sheet can be directed into the test section from the top window and fluorescence can be detected from the side. Also, the CCD camera can be placed very close to the test section windows, resulting in a working distance slightly larger than half of the test section width and allowing good-magnification (7 pixels/mm) PLIF images to be obtained without modification of the tunnel or using exotic camera optics. Furthermore, the tunnel was already equipped with windows composed of UV-grade fused silica, providing ~90% transmission at the 225 nm and higher wavelengths required for PLIF.

Test durations of up to 2 min are possible in this facility. Tests could be performed approximately once per hour. The facility stagnation pressure, P_o, can be varied from 350 (2.41) to 1450 psia (10.0 MPa) to simulate a range of Reynolds numbers [21]. Two different stagnation pressures were used in this experiment: 350 (2.41) and 720 psia (4.96 MPa), corresponding to freestream unit Reynolds numbers of 0.5 and 1.0×10^6/ft, respectively. The test core size varies from about 12×12 in.^{2} (0.30×0.30 m^2) at the lowest stagnation pressure to 14×14 in.^{2} (0.36×0.36 m^2) at the highest pressure [21]. The nominal stagnation temperature was 1800°R (1000 K) for the experiment described herein. The freestream temperatures are estimated to be between 90 and 95°R (50 and 53 K), depending on chosen operating conditions [21]. The freestream velocity is estimated to be about 4640 ft/s (1414 m/s) [21]. The freestream pressure was estimated to be 0.0099 psia (68 Pa) for the $P_o = 350$ psia condition and 0.0187 psia (129 Pa) for the $P_o = 720$ psia condition [21]. Model surface pressures were determined using electronically scanned pressure (ESP) piezoresistive silicon sensors connected by 4-ft-long tubes to the model.

This length contributed to a delayed time response. The fore- and aftbody pressure orifices were 0.040 and 0.060 in. in diameter, respectively. The 10 in. water column (0.36 psi) ESP module was enclosed in the tunnel injection box and, thus, was out of the airstream. The reference side of the module was held at a low vacuum pressure. At the lowest stagnation pressure conditions, ports on the aft side of the model took nearly 1 min to stabilize. Forebody pressures stabilized within a few seconds. Facility and model temperatures, pressures, angles of attack, etc., were recorded by a data acquisition system at a rate of 20 Hz.

At the time of this experiment, the 31 in. Mach 10 Tunnel facility was not equipped with a toxic gas cabinet for handling gas bottles containing NO. Because this was the first use of NO PLIF into this facility and long-term usage of the technique in the facility was not assured before performing the experiment, a safe and easy-to-implement but inefficient method was used to supply NO. A small ($\sim$0.5 l/$\sim$17 oz) vessel was pressurized with a 95% N_2, 5% NO mixture to $\sim$100 psia ($\sim$700 kPa). This small volume and fill pressure was used to minimize the quantity of NO gas that would have been present in the room in the event of a leak. If a leak had developed, the NO concentration would not have exceeded the Occupational Safety and Health Administration approved 8 hr time weighted average limit (25 ppm), assuming that all of the gas mixed/diffused into a 3 ft (1 m) radius around the leak. The gas bottle needed to be refilled after 3–5 tunnel runs. The NO/N_2 mixture flowed through mass flow controllers and then through the sting and into the model through stainless steel tubing embedded in the model. This tubing connected to the RCS jet nozzle. The mass flow controllers were made by Teledyne Hastings; the primary controller used in this experiment had a maximum flow rate of 1 standard liter per minute (slpm) and an accuracy of $\pm$(0.2% of full scale+ 0.5% of reading), or about 0.005 slpm for the conditions used. Nominal flow rates used in this experiment were 0.5 and 0.2 slpm. The flow rates were recorded by the data acquisition system at 20 Hz. One figure in the paper, as will be noted, shows much higher flow rates (up to 20 slpm) obtained in a subsequent test using a permanently installed gas supply system detailed in [22].

The normal sequence of the operation was to begin flowing the NO/N_2 mix through the RCS jet and then to begin the tunnel flow and wait until both flows stabilized; then the data acquisition was started, the model was injected into the flow, and the camera acquisition was started (sometimes more than once per run). A manual trigger indicated to the data acquisition system that the PLIF image acquisition had begun.

III. Analysis Methods

A. Planar Laser-Induced Fluorescence Flow Visualization Image Processing

Single-shot PLIF images were processed to subtract background scattered light and camera dark current, but the spatial variations in laser sheet intensity were not corrected. Both the background image and the single-shot images were smoothed with a filter (MATLAB®'s 3×3 pixel rotationally symmetric low-pass "fspecial()" Gaussian filter with a standard deviation of 1) before additional processing to reduce noise in the images. A background image was then subtracted from the filtered single-shot image. These images were then made into bitmap images or movies for display on the model using the Virtual Diagnostics Interface (ViDI) described in Sec. III.C. Some flow visualization images were subsequently processed to determine the jet centerline, as described in Sec. III.B, so that the trajectory and the flapping of the jet could be quantified.

B. Planar Laser-Induced Fluorescence Reaction-Control System Jet Trajectory Analysis

PLIF images of the RCS jet were analyzed to determine the centerline of the jet. Sets of 100 individual visualization images were processed with custom-written MATLAB® software previously used for velocimetry [19,23]. The images were first smoothed with MATLAB®'s 5×5 pixel Gaussian filter using a standard deviation of 2 pixels. Then each column in the image was fitted with a Gaussian function to determine the position of the jet within that column with subpixel accuracy. As the jet propagates downstream in the image, it spreads out and dissipates. When the signal intensity dropped below a preset threshold value, the fitting process was terminated to avoid fitting to noise. The measured trajectories were then converted from pixels into millimeters using the imaging system magnification, which was measured by imaging a scale. The magnification varied between 5 and 7 pixels/mm between the different images analyzed. For each column in the image, an average and a standard deviation of the jet centerline was determined from the 100 images. These averaged jet centerlines were then graphed with the origin of the graph located at the center of where the RCS jet exits the capsule.

C. Virtual Diagnostics Interface

ViDI [24] is a software package developed at NASA Langley Research Center that provides unified data handling and an interactive 3-D display of experimental and theoretical data. Currently, this technology is applied to three main areas: 1) pretest planning and optimization; 2) analysis and comparative evaluation of experimental and computational data in near real time or in postprocessing; and 3) establishment of a central hub to source, store, and retrieve experimental results. ViDI is a combination of custom applications and the 3-D commercial software Autodesk® 3ds Max®.[††]

For this experiment, ViDI was used for posttest visualization of PLIF and schlieren data. A CAD file for the Apollo capsule was imported into the virtual environment along with the PLIF and schlieren images. The images were then scaled and placed over the Apollo capsule. To create the final output, a virtual camera was placed in the scene and high-resolution bitmaps were rendered. In addition, a sequential series of files containing PLIF imagery was imported to create animations of time-varying data.

D. Conventional Data Systems

The surface pressure data were averaged over the last 2 s of each camera sequence (see earlier description of tunnel/data acquisition procedure). By this time, the pressures had reached a limiting value (i.e., were settled). The pressures were then converted to pressure coefficient $[C_p = (P - P_\infty)/q_\infty]$, where P_∞ and q_∞ are the freestream static and dynamic pressures, respectively. The 2σ uncertainty in C_p was estimated as ± 0.002, both from a propagation-of-errors method and from within-run and run-to-run repeatability.

IV. Results

Three parameters were varied in the experiment: 1) the mass flow rate of the RCS jet, 2) the stagnation pressure of the wind tunnel, and 3) the model angle of attack. Also, two different laser sheet orientations were used. These data sets are discussed individually in the following sections and then holistically in Sec. V.

A. Planar Laser-Induced Fluorescence and Schlieren Flow Visualizations

1. *Qualitative Interpretation*

Figure 3 shows a ViDI rendering of the capsule model with a single-shot false-color NO PLIF image overlaid. For this measurement, the laser sheet entered the flowfield from the top, was oriented parallel to the sting, and was on the model centerline. The camera was placed at a right angle to the laser sheet. Unless otherwise specified, all visualizations shown in this paper were obtained using this configuration. In the ViDI rendering, the virtual camera was oriented from about a 45 deg angle and above the model to better show the details of the model and the location of the laser sheet.

The rendering shows that the RCS jet is emitted from its nozzle normal to the model's aft surface. The seeded NO acts as a tracer of the RCS jet fluid, so that the observed PLIF flow patterns can be

[††]Data about Autodesk, Inc. available online at http://www.autodesk.com [retrieved Feb. 20, 2008].

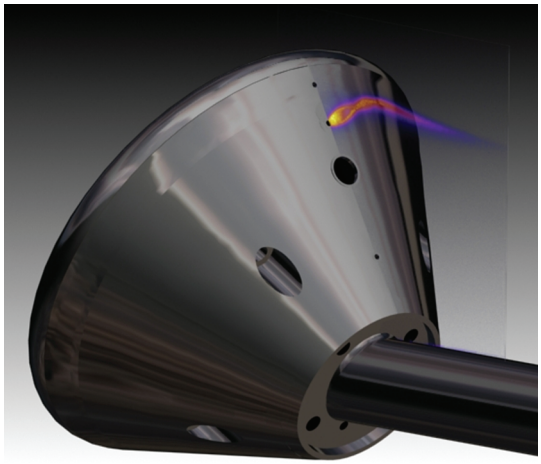

Fig. 3 ViDI rendering of the capsule model with PLIF visualization of the RCS jet.

considered streak lines, at least for the low jet flow rate cases. At the nozzle exit, the jet expands into a classic barrel shock pattern, clearly visible in the image, indicating that it is highly underexpanded. Downstream of this oval structure, the jet bends dramatically back toward the model centerline. The jet curves in this location because it is approaching the shear layer that separates the low-speed gas in the capsule's separated wake from the high-speed gas coming from the capsule's forebody. (A series of separate PLIF visualizations, not reported here but obtained at the same time as these, substantiates this claim.) As the jet propagates further downstream, it is observed to decrease in intensity. There are two main causes for this decrease in PLIF intensity. As will be shown, the jet is forming into a kidney shape. Thus, much of the jet gas is being transported away from the measurement plane. Because the fluorescence intensity is proportionate to the NO concentration, the signal decreases. The second effect is that O_2 from the tunnel gas is mixing with the jet gas on a molecular scale as the jet propagates. Because O_2 quenches the fluorescence of NO, the fluorescence signal decreases as more mixing occurs. Another possible cause for the decrease in the PLIF intensity is that the NO could be reacting with the air to be converted to NO_2. This effect will be studied in future work.

Figure 4 compares PLIF and schlieren for various operating conditions. The schlieren image in Fig. 4a clearly identifies the bow shock on the model. This figure shows an average of 20 single-shot schlieren images so that shot-to-shot variations are averaged out. The black marks randomly located around the image are caused by dirt and scratches on the optics in both the schlieren system and tunnel windows. For these schlieren measurements, the mass flow rate of NO from the RCS jet was 0.5 slpm, the maximum value used in this study. However, the jet cannot be seen in the schlieren image. It is possible that the sensitivity of the schlieren system could have been improved to visualize the jet, but clearly this flow visualization method does not easily visualize the jet in the present experiment. Another observation from the schlieren images was that the images obtained with the RCS jet flowing were indistinguishable from those with no RCS jet. That is, the forebody shock wave did not appear to change shape with fluid injection at this location. Figures 4c and 4d show single-shot schlieren images obtained at different times. Note that these single images have sharper shock waves than in the averaged image of Fig. 4a. Also, note the slightly different curvatures in the bow shocks in the two figures. This is typical of the observed small degree of bow-shock unsteadiness in the experiment.

Figure 4b shows the same PLIF visualization of the RCS jet shown in Fig. 3, but from a different virtual camera orientation and overlaid with schlieren. An inset to Fig. 4b shows a detailed view of the fluorescence intensity at the jet exit, clearly showing the barrel shock structure of the jet, although no Mach disk is observed from this supersonic jet. Figure 4d shows a PLIF image obtained with the same RCS jet mass flow rate but with the tunnel stagnation pressure about 2 times higher. Consequently, the observed underexpanded barrel shock is smaller (because the pressure ratio across the nozzle is smaller), though the general behavior of the flow is similar. In Fig. 4c, the operating conditions are the same as in Fig. 4d, except with a reduced RCS jet flow rate (0.2 slpm). Note the even-smaller barrel shock pattern (barely distinguishable); also, the jet does not appear to

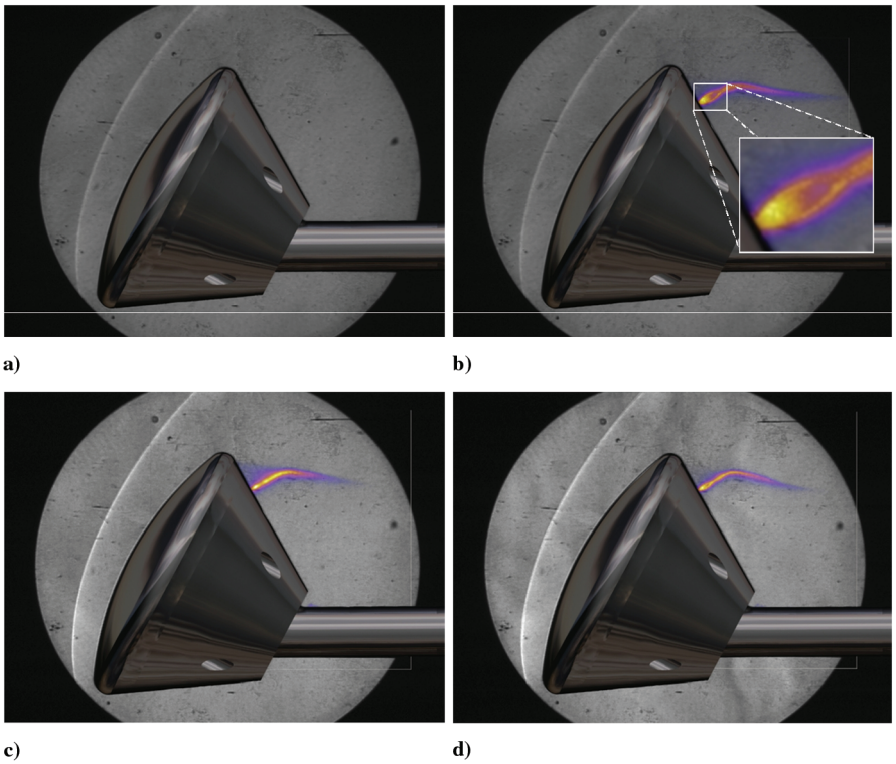

Fig. 4 PLIF and schlieren visualizations: a) $\dot{m} = 0.5$ slpm and $P_o = 350$ psia (schlieren only), b) $\dot{m} = 0.5$ slpm and $P_o = 350$ psia, c) $\dot{m} = 0.2$ slpm and $P_o = 720$ psia, and d) $\dot{m} = 0.5$ slpm and $P_o = 720$ psia.

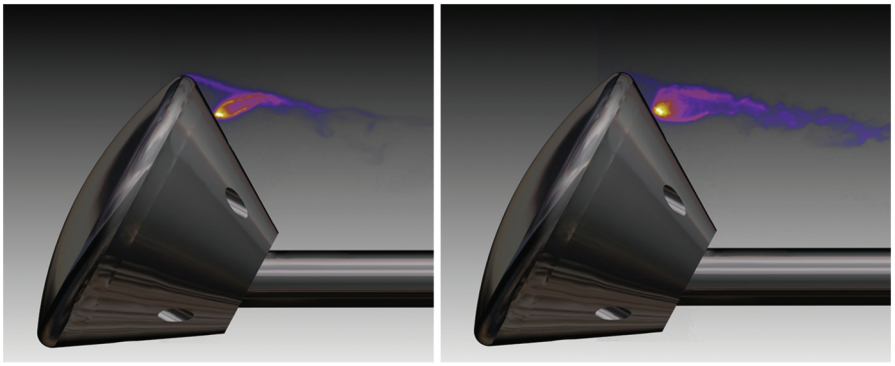

a) b)

Fig. 5 PLIF visualizations: a) $\dot{m} = 2.8$ slpm and $P_o = 1450$ psia, and b) $\dot{m} = 19.7$ slpm and $P_o = 1450$ psia.

penetrate as far into the shear layer. To summarize, the shape of the RCS jet plume near the exit depends on both the jet gas flow rate and the tunnel stagnation pressure, both of which affect the pressure ratio across the RCS jet nozzle.

To investigate RCS jets having higher mass flow rates, a permanent hazardous gas containment and supply system was installed near the 31 in. Mach 10 Tunnel. This allowed flow rates of NO-seeded N_2 to be delivered at up to 20 slpm. In this experiment, NO was also injected from a pressure port on the forebody of the model to visualize a streak line starting on the forebody and flowing around the shoulder of the model. This forebody flow was observed to be laminar if the RCS jet was not flowing. Figure 5 shows two images acquired with the RCS jets activated. Note that the diameter and length of the barrel shock is much larger in Fig. 5a than in any image in Fig. 4, and the barrel shock continues to grow as the flow rate is increased (see Fig. 5b). Furthermore, the flow becomes unsteady at these higher flow rates, resulting in transitional and turbulent flow structures. These two runs were obtained at a higher stagnation pressure and, consequently, the higher unit Reynolds number than those in Fig. 4. The higher Reynolds number encourages growth of these turbulent structures. A final observation from Fig. 5 is that the RCS jet does not appear to propagate far beyond the streak line emanating from the forebody surface.

The angle of attack of the model was varied from −15 to 0 deg during one 10 s run. This corresponds to the model angle of attack varying from 13 to 28 deg. A hand-pressed trigger was used to synchronize the PLIF acquisition to the angle of attack measurement in the data acquisition system. The accuracy in this manual timing is estimated to be about 0.5 s, which corresponds to about a 1 deg error in matching the sting angle with PLIF image. ViDI rendered these images into a movie showing the change in the shape of the jet during this sweep. Three still frames of this measurement are shown in Fig. 6, in which $P_o = 350$ psia and $\dot{m} = 0.5$ slpm. The shape and trajectory of the jet changes as the angle of attack varies.

Many flowfields are highly three dimensional, including this one. Imaging along the centerline of the model does not describe the flowfield fully. To systematically obtain measurements at other locations in this flow, the laser sheet was swept through the flow during some runs. The laser was still impinging on the model from above, and the width of the laser sheet was still parallel to the axis of the sting and the tunnel. However, the sheet no longer coincided with the centerline of the model. It was placed 10 mm to the far side of the jet centerline (from the camera's perspective) and was swept toward the camera at the rate of 2 mm/s. In 10 s, the entire three-dimensional flowfield was sampled. In postprocessing, one hundred 512×512 pixel images were converted into 512 100×512 pixel composite images. Figure 7 shows eight of these 100×512 pixel images overlaid on the model. These images show the evolution of the shape of the jet as it propagates downstream. The jet is observed to evolve from being round shaped near the nozzle exit (with the largest diameter inside the barrel shock) to being kidney shaped far from the nozzle. This is typical for a jet in a crossflow. No smoothing has been applied to these images.

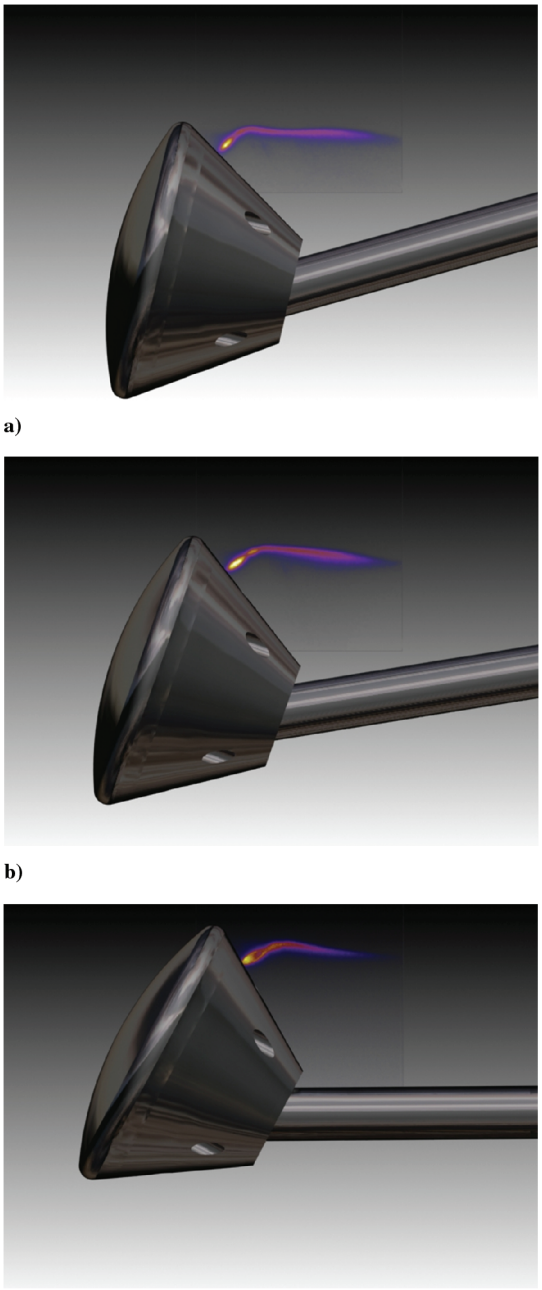

a)

b)

c)

Fig. 6 Angle-of-attack variation during a tunnel run: a) 13, b) 20, and c) 28 deg.

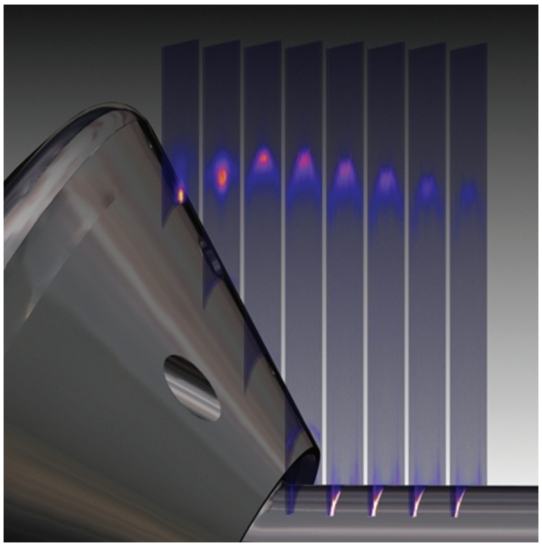

Fig. 7 ViDI rendering of eight equally spaced planes of data generated by sweeping the laser sheet, which was aligned parallel to the sting, spanwise through the flow.

To obtain a direct image of the cross section of the RCS jet, it was desired to orient the laser sheet perpendicular to the tunnel axis and to sweep the laser sheet along the tunnel axis while visualizing the fluorescence from a downstream location. This was not possible for practical reasons, including the fact that there is no optical port downstream. However, a compromise was obtained by orienting the laser sheet at a 45 deg angle with respect to the tunnel centerline and orienting the camera at a right angle to this sheet. As the laser sheet swept in the horizontal direction, different jet cross sections were intersected and visualized. Figure 8 shows some renderings obtained using this method. The four images are at four different laser sheet positions. Again, the jet is observed to evolve from being circular (elliptical in this view, because the laser sheet is at 45 deg with respect to the jet) to being kidney shaped.

2. *Quantitative Interpretation: Measured Jet Trajectories*

These flow visualization images provided quantitative information about the trajectory of the RCS jet into the laminar base flow for different operating conditions. The trajectories of the individual jets were determined using the method described in Sec. III.B. Figure 9 shows the measured trajectory for one operating condition. Note that the vertical and horizontal scales differ; the vertical scale has been expanded. The figure shows the averaged centerline position of the jet. The jet trajectory is approximately straight and perpendicular to the model surface near the nozzle exit, probably because it is propagating into a relatively quiescent (low-speed) separated flow region aft of the model. The jet then approaches the aforementioned shear layer, where it turns.

Figure 9 also shows the range over which the jet centerline fluctuates. A range of ± 2 standard deviations was plotted as thin curves to indicate the range of jet flapping during the 10 s measurement. The jet flapping increases as the jet propagates downstream from a negligible standard deviation of 0.03 mm at injection to a standard deviation of $\sim$0.9 mm at the maximum. The maximum standard deviation (0.9 mm) is comparable to, but smaller than, the jet plume diameter ($\sim$1.5–4 mm, measured full width at half-maximum). For comparison, the RCS nozzle exit diameter was 1.52 mm (0.060 in.). For the two runs in which 100 single measurements were obtained ($\dot{m} = 0.2$ and 0.5 slpm for $P_o = 720$ psia), the magnitude of the flapping was very similar: the maximum standard deviation was $\sim$0.9 mm for both runs.

Figure 10 compares the averaged jet trajectories for three different experimental conditions. A gap in the data is present in the region of the barrel shock for the 0.5 slpm, $P_o = 350$ psia run. The Gaussian fit

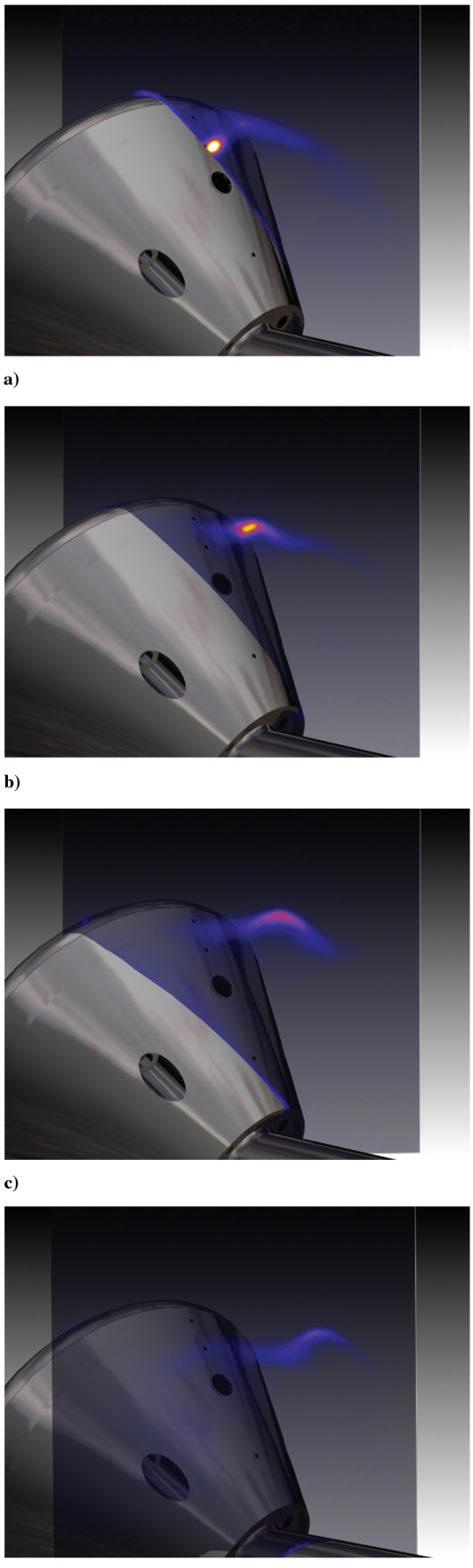

a)

b)

c)

d)

Fig. 8 Visualizations generated by orienting the laser sheet/camera system at 45 deg to the tunnel axis and sweeping the laser sheet spanwise through the flow.

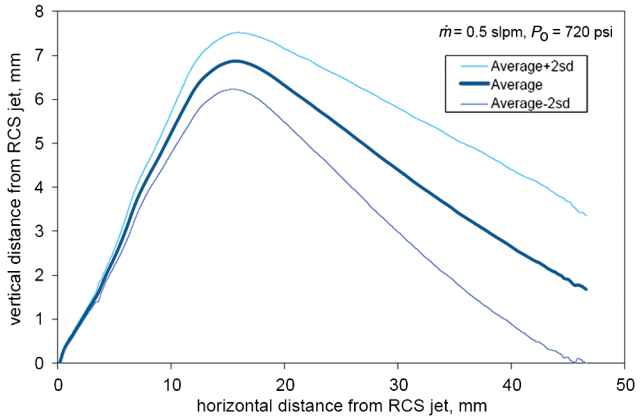

Fig. 9 Averaged jet centerline trajectory (thick curve) and jet centerline range caused by flapping.

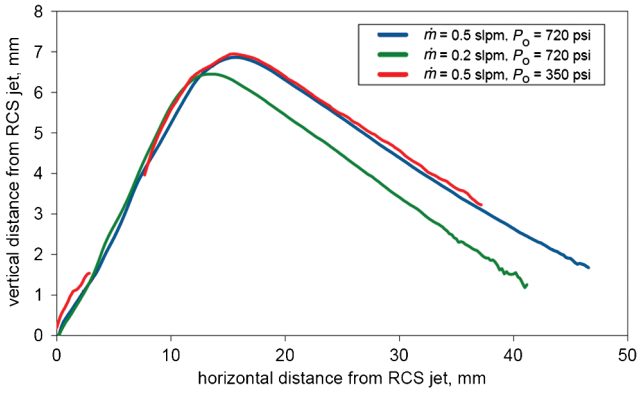

Fig. 10 Comparison of averaged jet trajectories for different experimental conditions.

algorithm could not fit the data in this region because the columns of data contained two peaks in intensity. This same effect may also be influencing the fitted trajectory near the nozzle exit (<8 mm horizontal distance) of the other two cases. Until the jet reaches the shear layer, the three different jets share approximately the same linear trajectory. The 0.5 slpm jets have very similar trajectories despite issuing into gas that has a different pressure by a factor of 2. As mentioned earlier, the size of the barrel shock differs in the two flow visualizations at the two different tunnel stagnation pressures. Because the flowfields are visibly different, it was not anticipated that the centerline trajectories would be so similar. Further testing is required to determine whether this is a general trend or a coincidence. Comparing the 0.2 and 0.5 slpm curves indicates that the jet with the higher flow rate (more momentum) penetrated deeper into the shear layer before turning, as expected.

The data in Fig. 9 have been superimposed on a ViDI rendering of the model in Fig. 11. This visualizes the jet trajectory in real spatial coordinates and also allows a double-check of the data in comparison with raw images.

B. Conventional Measurements

The surface pressure data are presented in Fig. 12 for a model angle of attack of 28 deg, $P_o = 720$ psia, corresponding to a unit Reynolds number of 1.06×10^6 and a mass flow rate of 0.5 slpm. On the horizontal axis, the distance, s, along the model has been normalized by the model radius, R_n, which is equal to 4.8 in. The RCS jet exhausted from port 3 ($s/R_n = 0.594$). No significant change in the surface pressures are noted when the RCS jet is operated at 0.5 slpm or lower. Figure 13 presents the same data but with an expanded scale on the vertical axis. Error bars shown are ± 2 standard deviations and are the same for each point, though they are only shown plotted on one run. For the two ports surrounding the RCS port, the surface pressures are slightly lower with the RCS jet active than inactive, though the difference is within the quoted uncertainty level.

It should be noted that the RCS jet was operated at low mass flow rates in the present experiment, which was aimed at demonstrating the NO PLIF measurement technique. Proper simulation of flight hardware may require much larger flow rates and thus may create greater interaction, though this would require substantial upgrades to the gas handling system. These data at low flow rates, however, indicate that it may be possible to seed NO into the flow for wake visualization studies using PLIF without altering the flow under investigation.

V. Discussion

The results show that the NO PLIF method can visualize RCS jet flows in hypersonic wind tunnels. Using image processing, including the ViDI visualizations, both qualitative and quantitative information can be obtained. This information should prove useful for validating the computational predictions of these flows. However, there were several lessons learned from this experiment. This section aims at identifying these lessons as well as suggesting solutions for problems experienced during the experiment.

The most important improvement that should be made to the system is to acquire images of a card with a regular pattern of dots each time the camera is moved or the lens is adjusted. The aptly named "dot card" should be placed in the plane of the laser sheet. The dot card has several uses. First, the spacing of the dots is carefully controlled so that the images can be dewarped, thereby correcting for lens distortions. Second, the magnification of the image can be accurately determined. Third, the dot card can help indicate where the PLIF images should be located relative to the model geometry in the ViDI renderings. This is particularly important in the case in which the laser is swept through the flowfield. In the present experiment, dot-card images were not acquired. Instead, images of a ruler were obtained for most runs to determine the image magnification. However, lens distortions may have caused the lens

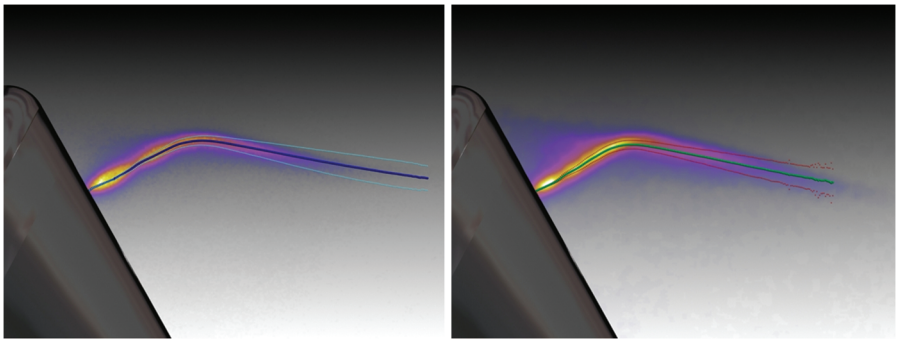

a) b)

Fig. 11 ViDI rendering of the measured jet centerlines (from Figs. 9 and 10) overlaid on typical single-shot PLIF images: a) $\dot{m} = 0.5$ slpm and $P_o = 720$ psia, and b) $\dot{m} = 0.2$ slpm and $P_o = 720$ psia.

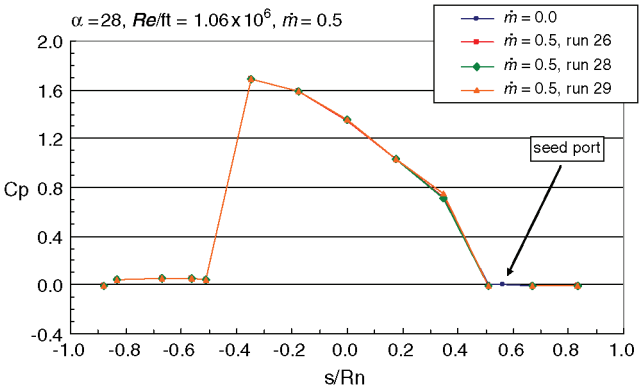

Fig. 12 Pressure coefficient distribution on the model for tunnel runs with $P_o = 720$ psia and varying $\dot{m}$.

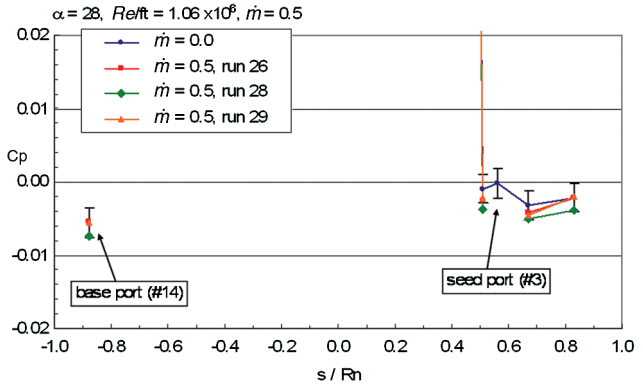

Fig. 13 Expanded scale of model pressure distribution, emphasizing aft-side orifices.

magnification to vary throughout the image. No adjustments were made for this effect in the present experiment. In some cases, the images were scaled by up to 5% to match to the rendered model. This image scaling could have been performed more systematically had a dot-card image been acquired. Similarly, in several of the experiments (see, for example, Fig. 8), it was not possible to determine exactly where the image plane was during ViDI processing. Assumptions were required and the images did not line up exactly with the model, as seen in Fig. 8a. In some cases, pressure ports or other model contours could be used as fiducial marks to assist in placing the images. Dot-card images will be acquired in future experiments. Before performing complicated experiments such as the one shown in Fig. 8, test runs should be performed in a carefully controlled laboratory experiment simulating a wind tunnel. This would allow systematic methods to be developed that would avoid errors in ViDI renderings.

Another problem that occurred in postprocessing the data was caused by using a manual trigger to document the start of a camera acquisition in the data file. This process has an uncertainty of about a half-second. During a dynamic event, such as an angle-of-attack sweep, a half-second of timing uncertainty can result in a 1 deg angle of attack uncertainty, that is, it is uncertain which image goes with which angle-of-attack measurement in the data file. This problem has since been resolved by using an electronic pulse (instead of a manual one) generated by the camera controller.

The accuracy of the jet trajectory measurement has not yet been carefully assessed. Clearly, the precision of the technique is sufficient to resolve flapping of these jets, at least far from the nozzle exit. The fitting algorithm is based on the one used in [19]. These researchers found that, when the signal-to-noise ratio was high, the fitting algorithm was accurate to $1/10$ of a pixel. In the present experiment, $1/10$ of a pixel corresponds to $\sim$0.02 mm (0.0008 in.). This is a reasonable estimate of the precision of the measurement in regions of the flow with high signal-to-noise ratio. However, lens distortions have not been corrected (and cannot be corrected for this data set), and so the accuracy of the measurement could be affected by such distortions. The lens distortions could be removed with image processing in future experiments if dot-card images are obtained before or after performing the experiments. Care was taken to align the camera so that the rows of the CCD were parallel to the sting. Typically, the camera rows were parallel to the sting to within a fraction of a degree. This was not a significant source of error in the experiments. The spatial resolution of the jet trajectory measurement was limited by the 5×5 pixel Gaussian smoothing algorithm, using a standard deviation of 2 pixels in MATLAB®. This process degrades the effective spatial resolution of the measurement to about 1 mm (that is, the measured centerline is averaged over a region of about 1 mm, though the position of this centerline could be determined to within 0.02 mm). In retrospect, the signal-to-noise ratio was good enough in the present data set that a much smaller filter, or perhaps no filter, could have been applied. Using a smaller filter, or no filter, would have improved the spatial resolution of the measurement by a factor of 4 or more. Another improvement to the software will be required to fit regions of the flow where the column of data does not have a Gaussian shape, such as in the barrel shock region of the jet. Finally, when the jet trajectory is not aligned perpendicular to the columns of the camera, a bias exists in the jet trajectory measurement. This is particularly a concern near the jet exit, where the jet is rapidly changing shape, for example, in the $\dot{m} = 0.2$, $P_o = 350$ psia case shown in Fig. 4b. Near the nozzle exit, the bottom of a given column corresponds to a location in the jet that is much closer to the nozzle exit than the top of the column. This has a tendency to bias the measured centerline data. It may instead be desirable to develop an algorithm that analyzes cross sections of the jet that are perpendicular to the jet. Nonetheless, when comparing the measure trajectories with the theoretical predictions, as long as the same method is used to find the theoretical jet centerline, the comparison should be valid.

VI. Conclusions

The planar laser-induced fluorescence technique has been applied to study a RCS jet on a capsule entry vehicle similar to Apollo and the proposed CEV. PLIF was used to visualize the jet, to determine the centerline trajectory of the jet, and to determine the shape of the jet downstream of injection. These measurements were complemented by conventional pressure instrumentation and schlieren bow-shock wave visualization. The experiment demonstrates the capabilities of PLIF as a nonintrusive measurement technique for studying RCS jets and provides a data set for comparison with CFD simulations of the flowfield. Improved confidence in CFD simulations should result in lower uncertainties in the operation of the RCS jets during flight.

Acknowledgments

We wish to acknowledge the contribution to this project from NASA Langley Research Center's 31 in. Mach 10 Tunnel technicians and engineers, including Anthony Robbins, Kevin Hollingsworth, Rhonda Murphy, Henry Fitzgerald, Johnny Ellis, and Paul Tucker. Also, we would like to acknowledge the contribution of Vince LeBoffe of NASA Langley Research Center for completing the model design. Finally, we would like to acknowledge Rich Schwartz from Swales Aerospace (now ATK) in Hampton, Virginia, for useful advice during the ViDI analysis.

References

[1] Anon., "NASA's Exploration Systems Architecture Study—Final Report," NASA TM-2005-214062; also http://www.nasa.gov/mission_pages/exploration/news/ESAS_report.html [retrieved 20 Feb. 2008].

[2] Sietzen, F., Jr., "From Mercury to CEV: Space Capsules Reemerge," *Aerospace America*, Vol. 43, No. 2, Feb. 2005, pp. 26–33.

[3] Vaughan, C. A., "Apollo Reaction Control Systems," AIAA Paper 68-566, 1968.

[4] Paul, P. H., Lee, M. P., and Hanson, R. K., "Molecular Velocity Imaging of Supersonic Flows Using Pulsed Planar Laser-Induced

Fluorescence of NO," *Optics Letters*, Vol. 14, No. 9, 1989, pp. 417–419.

[5] McMillin, B. K., Palmer, J. L., and Hanson, R. K., "Temporally Resolved, Two-Line Fluorescence Imaging of NO Temperature in a Transverse Jet in a Supersonic Cross-Flow," *Applied Optics*, Vol. 32, No. 36, 1993, pp. 7532–7545.

[6] Roberts, W. L., Allen, M. G., Howard, R. P., Wilson, G. J., and Trucco, R., "Measurement and Prediction of Nitric Oxide Concentration in the HYPULSE Expansion Tube Facility," AIAA Paper 94-2644, 1994.

[7] Ruyten, W. M., Smith, M. S., and Price, L. L., "Status of Laser-Induced Fluorescence and Planar Laser Induced Fluorescence Measurements in the AEDC HEAT-H2 Arc Heater Facility," AIAA Paper 95-2038, 1995.

[8] Ruyten, W. M., "Comparison of Calculated and Measured Temperature Fields in the AEDC Impulse Facility," AIAA Paper 1996-2237, 1996.

[9] Houwing, A. F. P., Palmer, J. L., Thurber, M. C., Wehe, S. D., Hanson, R. K., and Boyce, R. R., "Comparison of Planar Fluorescence Measurements and Computational Modeling of a Shock Layer Flow," *AIAA Journal*, Vol. 34, No. 3, 1996, pp. 470–477. doi:10.2514/3.13091

[10] Beck, W. H., Eitelberg, G., Trinks, O., and Wollenhaupt, M., "Testing Methodologies in the DLR High Enthalpy Shock Tunnel HEG," AIAA Paper 1998-2770, 1998.

[11] Fox, J. S., Houwing, A. F. P., Danehy, P. M., Gaston, M. J., Mudford, N. R., and Gai, S. L., "Mole-Fraction-Sensitive Imaging of Hypermixing Shear Layers," *Journal of Propulsion and Power*, Vol. 17, No. 2, 2001, pp. 284–292. doi:10.2514/2.5775

[12] Palma, P. C., Danehy, P. M., and Houwing, A. F. P., "Fluorescence Imaging of Rotational and Vibrational Temperature in a Shock Tunnel Nozzle Flow," *AIAA Journal*, Vol. 41, No. 9, Sept. 2003, pp. 1722–1732. doi:10.2514/2.7290

[13] Exton, R. J., Balla, R. J., Shirinzadeh, B., Hillard, M. E., and Brauckmann, G. J., "Wake Imaging in Supersonic Facilities Using the Iodine Cordes Bands," AIAA Paper 1998-2697, 1998.

[14] Hartfield, R. J., Jr., Hollo, S. D., and McDaniel, J. C., "Planar Temperature Measurement in Compressible Flows Using Laser-Induced Iodine Fluorescence," *Optics Letters*, Vol. 16, No. 2, 1991, pp. 106–108.

[15] Cecil, E., and McDaniel, J. C., "Planar Velocity and Temperature Measurements in Rarefied Hypersonic Flow Using Iodine LIF," AIAA Paper 2005-4965, June 2005.

[16] Staack, D., McDaniel, J. C., Glass, C. E., and Miller, C., "Experimental Study of Interacting Rarefied and Continuum Flows," AIAA Paper 2001-2762, June 2001.

[17] Shirinzadeh, B., Balla, R. J., and Hillard, M. E., "Rayleigh Scattering Measurements in Supersonic Facilities," AIAA Paper 96-2187, June 1996.

[18] Goyne, C. P., McDaniel, J. C., Krauss, R. H., and Day, S. W., "Velocity Measurement in a Dual-Mode Supersonic Combustor Using Particle Image Velocimetry," AIAA Paper 2001-1761, April 2001.

[19] Danehy, P. M., O'Byrne, S., Houwing, A. F. P., Fox, J. S., and Smith, D. R., "Flow-Tagging Velocimetry for Hypersonic Flows Using Fluorescence of Nitric Oxide," *AIAA Journal*, Vol. 41, No. 2, 2003, pp. 263–271. doi:10.2514/2.1939

[20] Wilkes, J. A., Alderfer, D. W., Jones, S. B., and Danehy, P. M., "Portable Fluorescence Imaging System for Hypersonic Flow Facilities," *JANNAF Interagency Propulsion Committee Meeting*, Chemical Propulsion Information Analysis Center, The Johns Hopkins Univ., Columbia, MD, Dec. 2003.

[21] Micol, J. R., "Langley Aerothermodynamic Facilities Complex: Enhancements and Testing Capabilities," AIAA Paper 98-0147, Jan. 1998.

[22] Alderfer, D. W., Danehy, P. M., Wilkes Inman, J. A., Berger, K. T., Buck, G. M., and Schwartz, R. J., "Fluorescence Visualization of Hypersonic Flow Over Rapid Prototype Wind-Tunnel Models," AIAA Paper 2007-1063, Jan. 2007.

[23] Miles, R. B., Grinstead, J., Kohl, R. H., and Diskin, G., "The RELIEF Flow Tagging Technique and Its Application in Engine Testing Facilities and for Helium–Air Mixing Studies," *Measurement Science and Technology*, Vol. 11, No. 9, Sept. 2000, pp. 1272–1281. doi:10.1088/0957-0233/11/9/304

[24] Schwartz, R. J., "ViDI: Virtual Diagnostics Interface Volume 1—The Future of Wind Tunnel Testing," NASA CR-2003-212667, Dec. 2003.

T. Lin
Associate Editor